minerals

MDPI

Article

Critical Metal Potential of Tasmanian Greisen: Lithium, Rare Earth Elements, and Bismuth Distribution and Implications for Processing

Julie Hunt [1,*], Jeffrey Oalmann [1,2], Mohamed Aâtach [3], Eric Pirard [3], Russell Fulton [4] and Sandrin Feig [5]

[1] CODES, School of Natural Sciences, University of Tasmania, Hobart, TAS 7000, Australia; jeffrey.oalmann@utas.edu.au
[2] CODES, Analytical Laboratories, University of Tasmania, Hobart, TAS 7000, Australia
[3] GeMMe, School of Engineering, University of Liege, 4000 Liege, Belgium; mohamed.aatach@uliege.be (M.A.); eric.pirard@uliege.be (E.P.)
[4] Tin One, Hobart, TAS 7000, Australia
[5] Central Science Laboratory, University of Tasmania, Hobart, TAS 7000, Australia; sandrin.feig@utas.edu.au
* Correspondence: julie.hunt@utas.edu.au

Abstract: Typical greisen-type ore samples from northeastern Tasmania were investigated for their critical metal potential. The samples contain zinnwaldite ($KLiFe^{2+}Al(AlSi_3O_{10})(F,OH)_2$), a lithium-bearing mica that is prone to excessive breakage during conventional processing, leading to the generation of very-fine-sized particles (i.e., slimes, <20 µm), eventually ending up in tailings and resulting in lithium (Li) loss. To assess whether the natural grain size of valuable minerals could be preserved, the samples were processed using electric pulse fragmentation (EPF). The results indicate that EPF preferentially fragmented along mica-rich veins, maintaining coarse grain sizes, although a lower degree of liberation was observed in fine-grained, massive samples. In addition, the critical metal distribution within zinnwaldite was examined using laser ablation inductively coupled plasma mass spectrometry (LA-ICP-MS) techniques. The results reveal differences in Li content between groundmass zinnwaldite and vein-hosted zinnwaldite and that the zinnwaldite contains the critical elements rubidium (Rb), cesium (Cs), and rare earth elements (REEs: La, Ce, Pr, and Nd). Vein-hosted zinnwaldite has a higher average Li content, whereas groundmass mica contains higher concentrations of Rb, Cs, and REEs. Both mica types host inclusions of bismuth–copper–thorium–arsenic (Bi-Cu-Th-As), which are more abundant in vein-hosted mica. In some of the samples, Bi, Cu, Th, and REEs also occur along the mica cleavage planes, as well as in mineral inclusions. The Li, Rb, and Cs grades are comparable to those of European deposits, such as Cínovec and the Zinnwald Lithium Project.

Keywords: lithium; zinnwaldite; critical metals; electric pulse fragmentation

Academic Editors: Rodrigo Magalhães de Carvalho, Glenn Bark and Alan R. Butcher

Received: 26 February 2025
Revised: 12 April 2025
Accepted: 25 April 2025
Published: 29 April 2025

Citation: Hunt, J.; Oalmann, J.; Aâtach, M.; Pirard, E.; Fulton, R.; Feig, S. Critical Metal Potential of Tasmanian Greisen: Lithium, Rare Earth Elements, and Bismuth Distribution and Implications for Processing. *Minerals* **2025**, *15*, 462. https://doi.org/10.3390/min15050462

1. Introduction

Lithium (Li) is a vital component of modern technologies, particularly for rechargeable batteries used in transportation and energy storage. The demand for Li is rising rapidly, while the supply remains limited and concentrated in a few countries. For example, Australia, Chile, and China together account for 90% of global production [1,2]. As a result, Li is listed as a critical mineral by Australia, the European Union, and the United States [3–5]. Lithium can be extracted from various natural sources, including Li-bearing micas hosted in greisen-type deposits, such as the well-known Zinnwald deposit in Europe. The samples from eastern Tasmania, included in this study, are greisen-type with Li occurring within

zinnwaldite ($KLiFe^{2+}Al(AlSi_3O_{10})(F,OH)_2$), a Li-bearing mica. The Li grades of these samples are similar to those reported for European deposits that have been historically mined or are currently under development, such as Cínovec (0.48% Li_2O; ~2230 ppm Li, [6]) and the Zinnwald Lithium Project (0.54% Li_2O; ~2500 ppm Li, [7]).

Zinnwaldite is a soft mineral that tends to break during conventional comminution, generating ultra-fine particles (<20 μm) that are difficult to recover using typical flotation methods and often end up in tailings. Although modified flotation processes have had some success in recovering the fine material (e.g., Cínovec [8]), Li losses remain significant. Coarse-grained mica is generally more amenable to processing, offering advantages such as reduced energy requirements for liberation, lower losses of valuable minerals to slimes (<10 μm), and reduced environmental impact of tailings, e.g., [9]. To explore this, this study employed electric pulse fragmentation (EPF), a technique that promotes fragmentation along grain boundaries and limits fine production [10–12]. Previous studies [13,14] have shown that EPF can preserve delicate mineral textures, such as surface growth features of platinum-group minerals, pyrite molds of microfossils, and separation of fossils from an asphalt matrix, while improving mineral liberation, including in cases where mechanical methods produce up to 45% fines (<80 μm) compared to only 5% with EPF [12]. Although the feasibility of using electric pulses for fragmentation to produce mineral separation has been investigated since at least the late 1960s, e.g., [13,14], interest has resurged since the 1990s [10,11,15–18]. A detailed development summary is provided in [15,17]. Key advantages of EPF over mechanical fragmentation methods include the following: preserving the natural grain size of minerals, minimizing fine generation, and producing fewer multi-mineral grains. This study investigates whether EPF can effectively liberate zinnwaldite in Tasmanian greisen ores without producing excessive fines.

A second objective was to assess the distribution of valuable additional elements in zinnwaldite and to determine potential differences between vein-hosted and groundmass occurrences. To achieve this, laser ablation inductively coupled plasma mass spectrometry (LA-ICP-MS) was used to quantify these elements, including rubidium (Rb), cesium (Cs), rare earth elements (REEs), and bismuth (Bi), which may have potential as co- or by-products.

2. Materials and Methods

2.1. Samples

Samples were collected from historic workings near the former Aberfoyle mine in northeastern Tasmania [19–21]. These were provided to the Centre for Ore Deposits and Earth Sciences (CODES), University of Tasmania (UTAS), for analysis; they are interpreted to be part of the Gipps Creek Granite (Ben Lomond Batholith). The samples consist predominantly of quartz, topaz, and mica ± tourmaline. Those tested using EPF include the following: hard, dense rock described in the field as finely crystalline, massive greisen (GM10339, GM10365); and finely crystalline, massive greisen cross-cut by vein-forming coarsely crystalline mica (GM10358). The samples were originally large rock blocks, which were cut into cubes for the comminution experiments—example images are provided in Section 3. imilar material was also used to determine the optimal processing parameters for EPF.

2.2. Geochemistry

Geochemical data from a regional exploration program (provided by [21]) indicate that the Li values in the samples correlate with elements such as Cs, Fe, Mn, Rb, Sc, Tl, and Zn (Figure 1). Among these, Cs and Rb are classified as critical elements in the USA, while Sc is listed as critical in both Australia and the USA [3,5]. The Li, Rb, and Cs grades of these

samples are comparable to those of deposits in Europe that have been historically mined or are currently under development, such as Cínovec and the Zinnwald Lithium Project, e.g., [6,7,22].

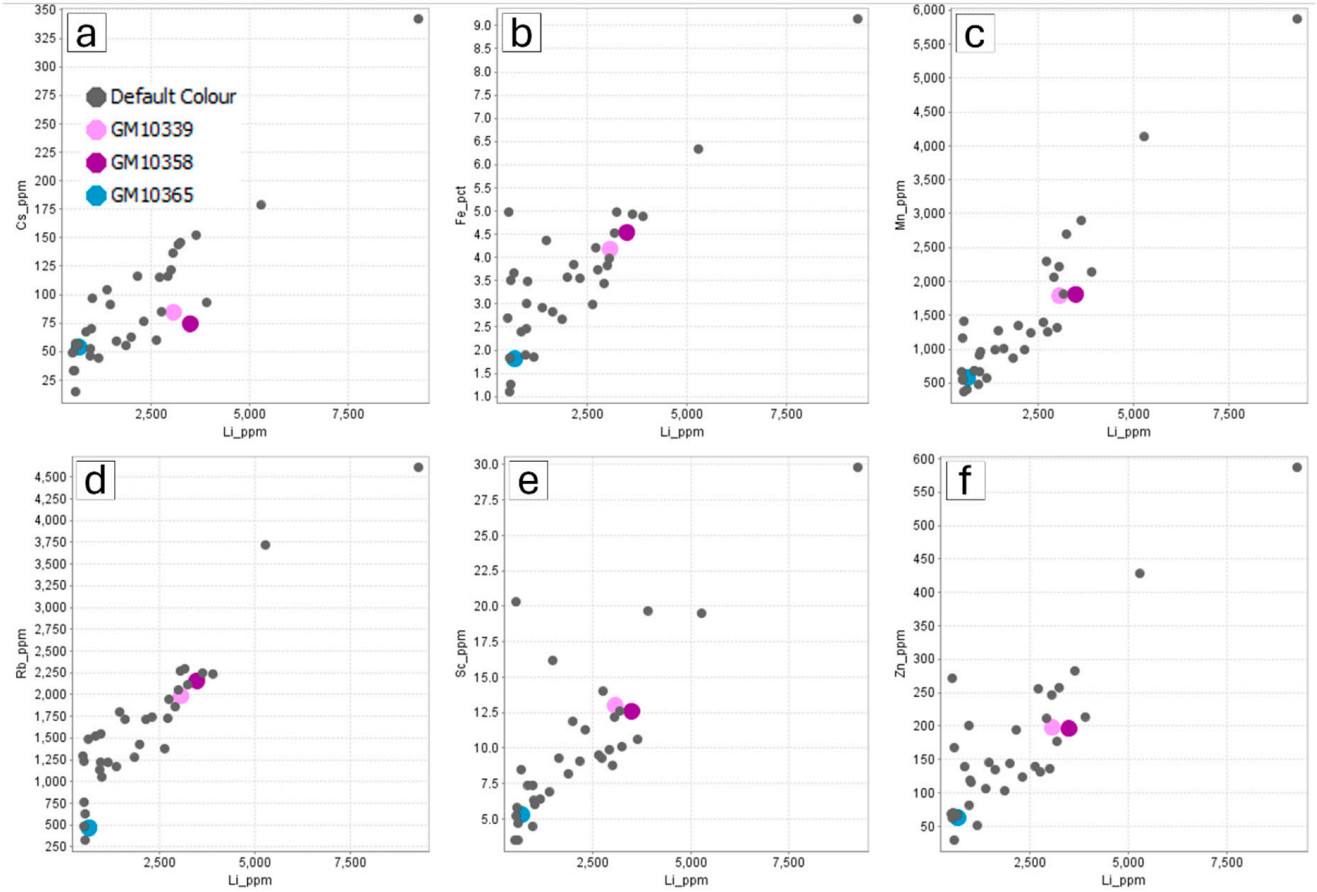

Figure 1. Geochemical analysis results for rock samples from the Aberfoyle area. Samples used in the EPF experiments are highlighted using large, colored symbols. The dataset has beenfiltered to display only samples with > 500 ppm Li (n = 35). Plots show the following: (**a**) Li vs. Cs; (**b**) Li vs. Fe; (**c**) Li vs. Mn; (**d**) Li vs. Rb; (**e**) Li vs. S; and (**f**) Li vs. Zn.

2.3. Methods

2.3.1. Comminution—Electric Pulse Fragmentation (EPF)

Fragmentation was performed using an SELFRAG Lab unit (SELFRAG AG, Kerzers, Switzerland), installed at the University of Liège (ULiège), within the 'Georesources, Mineral Engineering and Extractive Metallurgy' (GeMMe) group (Figures 2 and 3; [23]). This laboratory-scale system, as well as larger-scale devices (up to 8000 tpa), uses high-voltage electrical pulses in a dielectric medium to fragment solid composite materials, exploiting differences in electrical conductivity between materials. This typically results in liberation along grain boundaries. More details on SELFRAG operation can be found, for example, in [18] and on the SELFRAG website [23]. The samples were cut to ensure they would fit into the process vessel (maximum size: 4 × 4 × 4 cm), which was used in a closed configuration to retain all sample material within the vessel. During the fragmentation, deionized water was used as the dielectric medium to facilitate electrical discharge and minimize sample contamination.

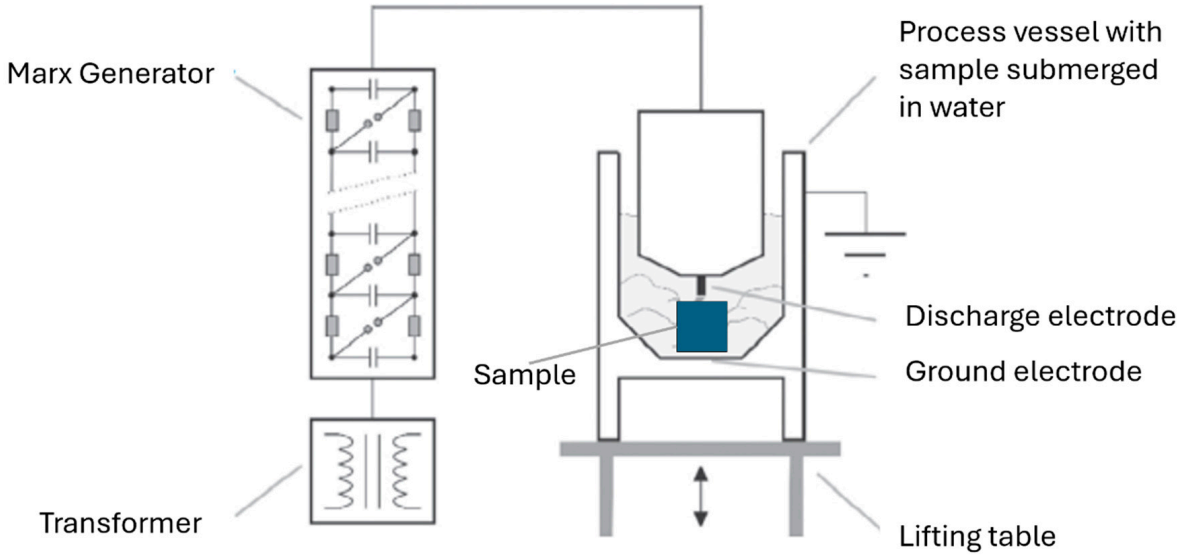

Figure 2. Schematic diagram of the SELFRAG Lab unit (adapted from [18]).

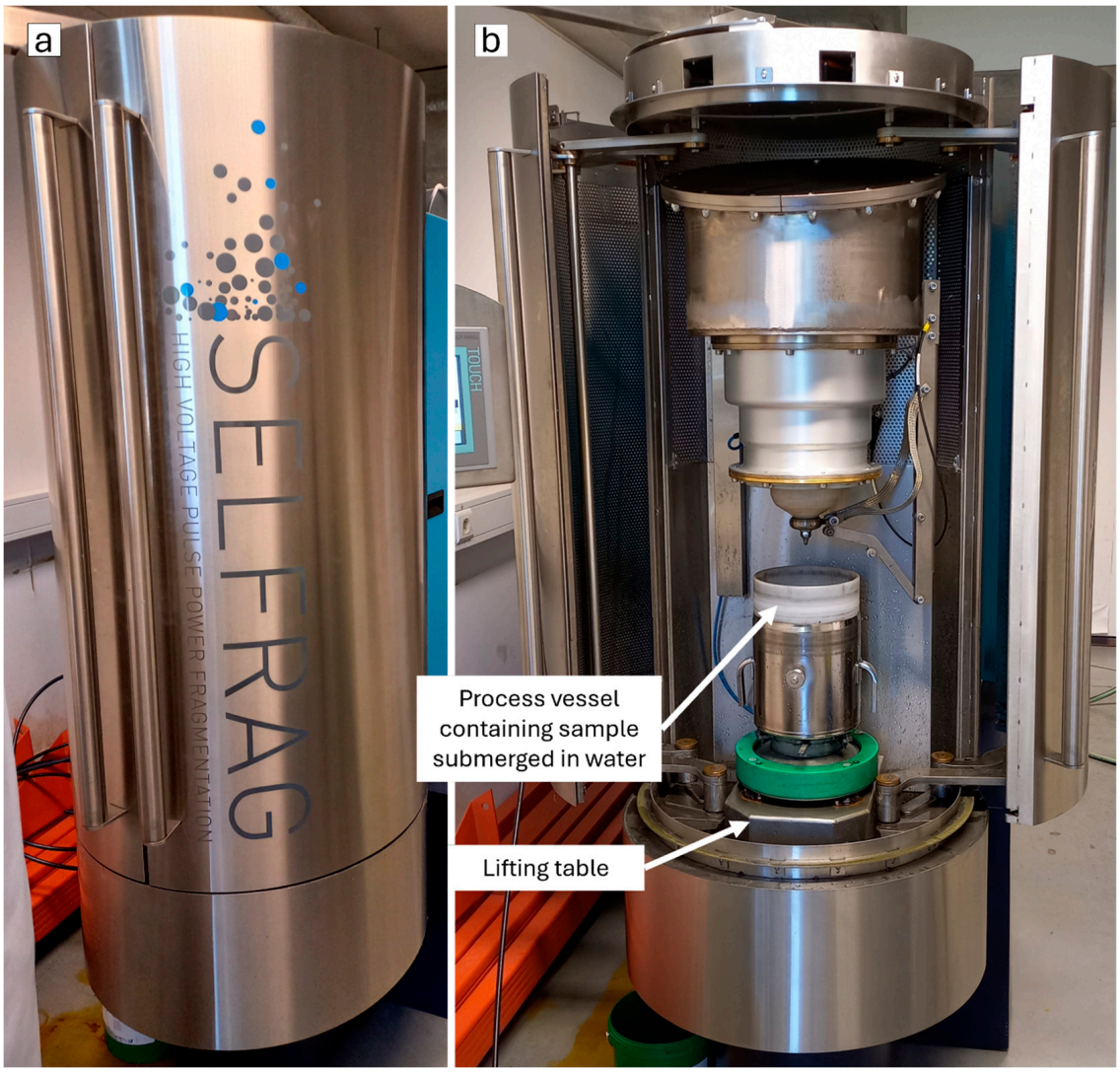

Figure 3. SELFRAG Lab unit installed at the GeMMe research group, University of Liège. (**a**) Unit in operational mode with the doors closed. (**b**) Unit with the doors open and lifting table lowered for sample loading.

Parameters including voltage, electrode gap, pulse rate, and number of electrical pulses can be adjusted in the SELFRAG Lab unit. Several pieces of each sample were tested, with the first pieces used as calibration samples to determine the appropriate experimental settings. The final settings are shown in Table 1, alongside the available range for each parameter. The experimental settings were chosen to retain the natural size of coarse minerals while still ensuring substantial rock breakage. Each fragmented sample was recovered in full by filtering the process and rinse water. Finally, the samples were dried overnight in a low-temperature (~65 °C) forced-air drying oven.

Table 1. Experimental settings used in the SELFRAG Lab unit for each sample, along with the available range for each parameter.

Sample	Voltage (kV)	Electrode Gap (mm)	Pulse Rate (Hz)	Number of Pulses
GM10339	120	30	5	60
GM10358	120	30	5	30
GM10365	200	40	5	10
Range	90 to 200	10 to 40	1 to 5	1 to >1000

2.3.2. Mineralogy—Scanning Electron Microscope (SEM)-Based Automated Mineralogy

Coarse-sized material was embedded in resin mounts, polished, and analyzed using an FEI MLA 650 SEM, equipped with two Bruker XFlash 5030 detectors, operating at 20 kV and 7 nA, at the Central Science Laboratory, University of Tasmania, Australia. Mineralogical data (e.g., size, liberation, and association) were obtained using the automated Advanced Mineral Identification and Characterization System (AMICS) software, version 3.3.0.1701 [24].

2.3.3. Element Distribution—LA ICP-MS

The resin mounts used for mineralogy were analyzed using LA-ICP-MS at the CODES Analytical Laboratories, University of Tasmania. Spot analyses were conducted on a Resolution SE laser ablation system with an ATL ATLEX-I LR ArF excimer laser operating at a wavelength of 193 nm and pulse width of ~5 ns, coupled with an Agilent 8900 quadrupole mass spectrometer. The analyses were performed in time-resolved mode. The sample ablation was performed in a He atmosphere flowing at 0.35 L/min and immediately combined with Ar flowing at 1.05 L/min. Before each analysis, 5 pre-ablation shots were used to 'clean' the surface of any contaminants, followed by a 20 s 'washout' delay. Each analysis began with a 30 s blank gas measurement, followed by a further 60 s of analysis time when the laser was switched on. The ablation spot size was set to a 30 µm diameter with the frequency set at 5 Hz and a laser fluence of 3.5 J/cm^2. The trace element abundances were calibrated against the NIST612 glass using values of [25], and secondary standard corrections using analyses of the glasses BCR-2G and GSD-1G based on [26] preferred values. The primary standard NIST612 was analyzed at a beam size of 60 µm and 10 Hz frequency, while the secondary standards GSD-1G and BCR-2G were analyzed at the same conditions as the zinnwaldite. The standards were run throughout the analytical session for drift correction, calibration, quantification, and secondary correction.

The ICPMS was tuned to maximize sensitivity while maintaining a U/Th of ≈1.05 during a line scan (3 µm/s) ablation of the NIST612 glass. The production of molecular oxide species (i.e., $^{232}Th^{16}O/^{232}Th$) was maintained at levels below 0.2%, while doubly-charged ion species production (i.e., $^{44}Ca^{2+}/^{44}Ca^{+}$) was kept under 0.2% while ablating the line scan with a 40 µm round beam at 10 Hz and a 3.5 J/cm^2 laser beam fluence.

The following isotopes were measured in the zinnwaldite and the primary and secondary standards: ^{7}Li, ^{9}Be, ^{23}Na, ^{24}Mg, ^{27}Al, ^{29}Si, ^{31}P, ^{35}Cl, ^{39}K, ^{43}Ca, ^{47}Ti, ^{49}Ti, ^{51}V, ^{53}Cr, ^{55}Mn, ^{57}Fe, ^{59}Co, ^{60}Ni, ^{65}Cu, ^{66}Zn, ^{71}Ga, ^{72}Ge, ^{75}As, ^{85}Rb, ^{88}Sr, ^{89}Y, ^{90}Zr, ^{93}Nb, ^{95}Mo, ^{107}Ag, ^{109}Ag, ^{118}Sn, ^{12}1Sb, ^{133}Cs, ^{137}Ba, ^{139}La, ^{140}Ce, ^{141}Pr, ^{146}Nd, ^{147}Sm, ^{153}Eu, ^{157}Gd, ^{159}Tb, ^{163}Dy, ^{165}Ho, ^{166}Er, ^{169}Tm, ^{172}Yb, ^{175}Lu, ^{178}Hf, ^{181}Ta, ^{182}W, ^{197}Au, ^{205}Tl, ^{206}Pb, ^{207}Pb, ^{208}Pb, ^{209}Bi, ^{232}Th, ^{238}U. Data reduction was performed according to the methods established by [27] using LADR v1.1.07 software [28]. Quantification was performed using ^{27}Al as the internal standard element, normalizing all measured cations to the oxide total of 100%, with oxygen calculated stoichiometrically rather than being measured. The data were filtered by selecting time intervals from the 60 s acquisition that did not include mixing with other minerals. The remaining intervals were then sub-divided to identify those containing inclusions. The interval selection was performed visually via the LADR software.

2.3.4. Element Mapping—LA ICP-TOF-MS

Major and trace element maps of zinnwaldite were produced using laser ablation inductively coupled plasma time-of-flight mass spectrometry (LA-ICP-TOF-MS) at CODES Analytical Laboratories, University of Tasmania. The laser ablation system used for the mapping consists of the same resolution SE laser ablation system used for the spot analyses coupled to a Tofwerk (Thun, Switzerland) icpTOF R time-of-flight mass spectrometer. However, a smaller-volume funnel PEEK tubing was used to mix the He plus ablated sample with Ar, and PEEK tubing with a 1 mm inner diameter was used to transport the sample aerosol to the plasma. This hardware configuration allowed the signal to wash out to <10% of the maximum intensity within 100 ms. The sample ablation was performed in a He atmosphere flowing at 1.0 L/min and immediately combined with Ar flowing at 1.05 L/min in the small-volume funnel. A fluence of 3.5 J/cm^2, a laser repetition rate of 10 Hz, a square spot size of 9 µm by 9 µm, and a scan speed of 90 µm/s were used on all samples and reference materials in the line-scan mode. The mass spectrometer was triggered by each individual laser pulse to collect and sum 2000 full mass spectra, resulting in a total acquisition time of 60 ms for each data point. Under these parameters, each laser pulse corresponds to a single data point, which makes up a single map pixel without any overlapping pixels.

The ICP-TOF-MS was tuned to maximize sensitivity while maintaining a U/Th of ≈1.05 during a line scan (3 µm/s) ablation of the NIST612 glass. The production of molecular oxide species (i.e., ^{232}Th^{16}O/^{232}Th) was maintained at levels below 0.7%, while doubly-charged ion species production (i.e., ^{44}Ca^{2+}/^{44}Ca^{+}) was kept under 0.2%.

The spectral baseline for each data point was calculated and subtracted from each data point using Tofwerk's Tofware software, running in Igor Pro v. 7 (WaveMetrics, Portland, OR, USA), and a total of 62 peaks were integrated and exported as time series of counts per second for each of the following isotopes: ^{23}Na, ^{24}Mg, ^{27}Al, ^{29}Si, ^{31}P, ^{34}S, ^{35}Cl, ^{39}K, ^{43}Ca, ^{44}Ca, ^{45}Sc, ^{49}Ti, ^{51}V, ^{53}Cr, ^{55}Mn, ^{56}Fe, ^{57}Fe, ^{59}Co, ^{60}Ni, ^{63}Cu, ^{66}Zn, ^{71}Ga, ^{72}Ge, ^{75}As, ^{77}Se, ^{85}Rb, ^{88}Sr, ^{89}Y, ^{91}Zr, ^{93}Nb, ^{95}Mo, ^{109}Ag, ^{111}Cd, ^{118}Sn, ^{121}Sb, ^{125}Te, ^{137}Ba, ^{139}La, ^{140}Ce,^{141}Pr, ^{146}Nd, ^{147}Sm, ^{153}Eu, ^{157}Gd, ^{159}Tb, ^{163}Dy, ^{165}Ho, ^{166}Er, ^{169}Tm, ^{172}Yb, ^{175}Lu, ^{178}Hf, ^{181}Ta, ^{182}W, ^{197}Au, ^{203}Tl, ^{206}Pb, ^{207}Pb, ^{208}Pb, ^{209}Bi, ^{232}Th, ^{238}U. Note that data for mass-charge ratios less than 20 have not been obtained due to the extremely short flight times of these ions within the mass analyzer. Data reduction was performed using LADR software [28]. Element abundances for all elements, except K, were calibrated against analyses of NIST610 using the values of [25], while K was calibrated against BCR-2G glass using the [26] preferred value. The quantification was performed using ^{27}Al as the internal standard element, normalizing all measured cations to an oxide total of 91.79%, with oxygen calculated stoichiometrically. The total accounts for the inability to measure Li

and H, where the stoichiometric value of OH for pure zinnwaldite and the average Li_2O content from the spot analyses were implemented. For each map, a grid of pixel values in elemental weight percent was exported from LADR for each element. The maps were then constructed using an in-house script written in Python.

3. Results

3.1. Electric Pulse Fragmentation (EPF)

The EPF technique successfully fragmented the greisen samples, as illustrated in Figure 4, which shows example images of the results before and after EPF. From the images, it is clear that the original coarse size of the mica grains in the cross-cutting veins was preserved (Figure 4b). article size distribution analyses show that 79 to 89% of the sample mass remained in size fractions ≥250 µm after EPF; for two samples, 68 to 74% of the mass was retained in the >1.18 mm fraction (Table 2; Figure 5).

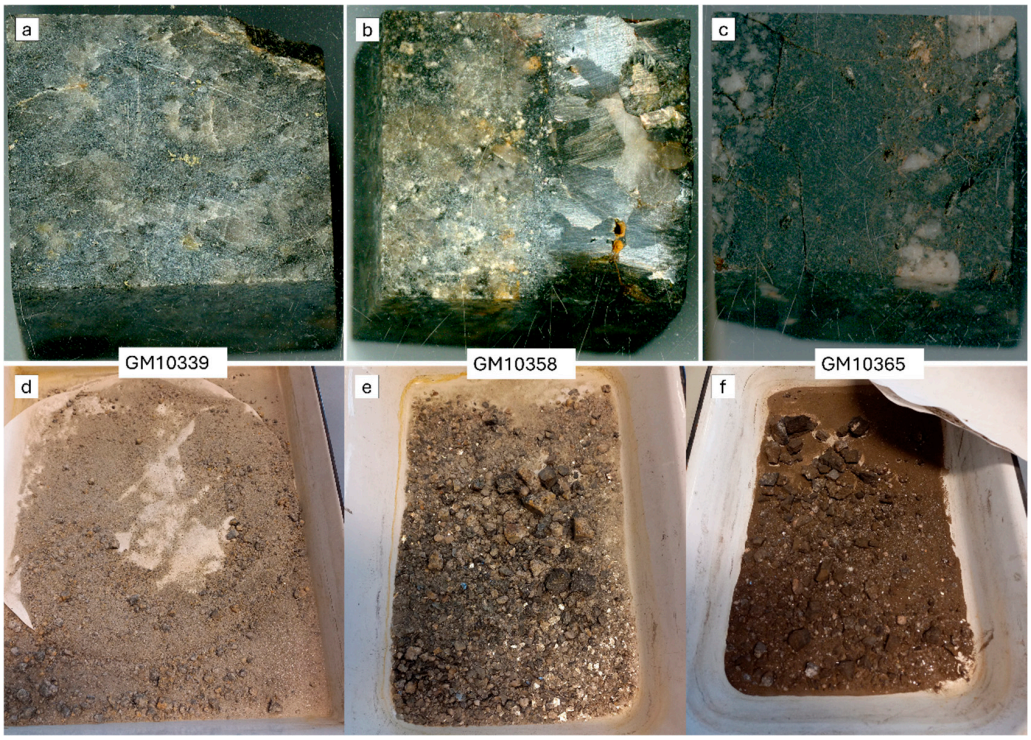

Figure 4. Example images of samples before (**a**–**c**) and after (**d**–**f**) EPF. Breakage conditions are provided in Table 1. Images (**a**–**c**): ~4 × 4 cm rock cubes. Images (**d**–**f**): the tray is 200 mm wide. GM10339 and GM10365: hard, dense, finely crystalline massive greisen; GM10358: finely crystalline massive greisen cross-cut by vein-forming coarsely crystalline mica.

Table 2. Mass percentage of each size fraction after dry sieving of EPF products. Bold values indicate the size fractions that account for the majority of the mass in each sample.

Sieve Size % Mass	GM10339	GM10358	GM10365
4 mm	11.5	**39.7**	**58.2**
2 mm	11.7	17.8	10.8
1.18 mm	10.4	10.9	5.5
500 µm	**24.3**	12.8	6.1
250 µm	**21.2**	8.2	3.2
125 µm	14.8	6	8.8
63 µm	3.4	2.3	4.7
<63 µm	2.7	2.1	2.7

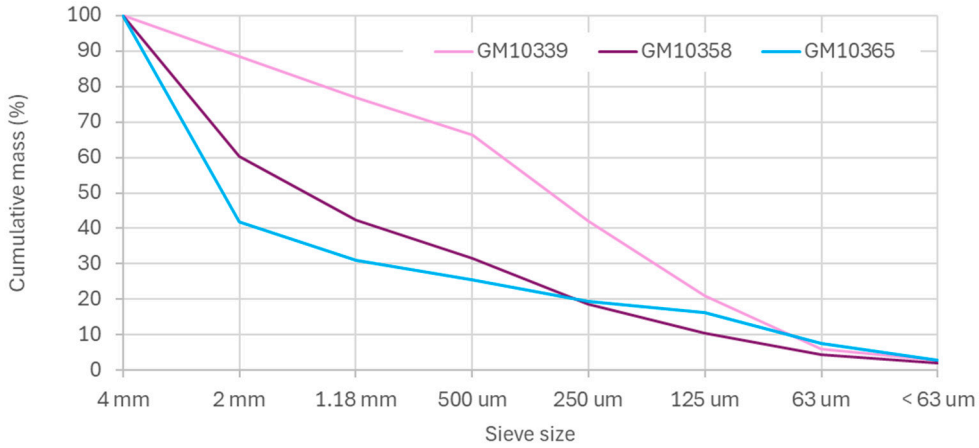

Figure 5. Cumulative mass percentage of EPF products after dry sieving.

3.2. Mineralogy—Abundance, Liberation, and Association

3.2.1. Abundance

SEM-based automated mineralogy shows that the samples consist mainly of zinnwaldite, quartz, topaz, and muscovite-illite ± tourmaline (schorl). The mineral proportions are summarized in Table 3 and illustrated in Figure 6.

Table 3. Weight percentages of minerals in the grain mounts shown in Figure 6.

Mineral (Weight %)	GM10339	GM10358	GM10365
Zinnwaldite	27.43	42.28	12.25
Quartz	59.3	48.88	37.24
Topaz	11.53	7.81	1.68
Tourmaline (schorl)	0.01	0	44.16
Muscovite-illite	0.26	0.27	3.06

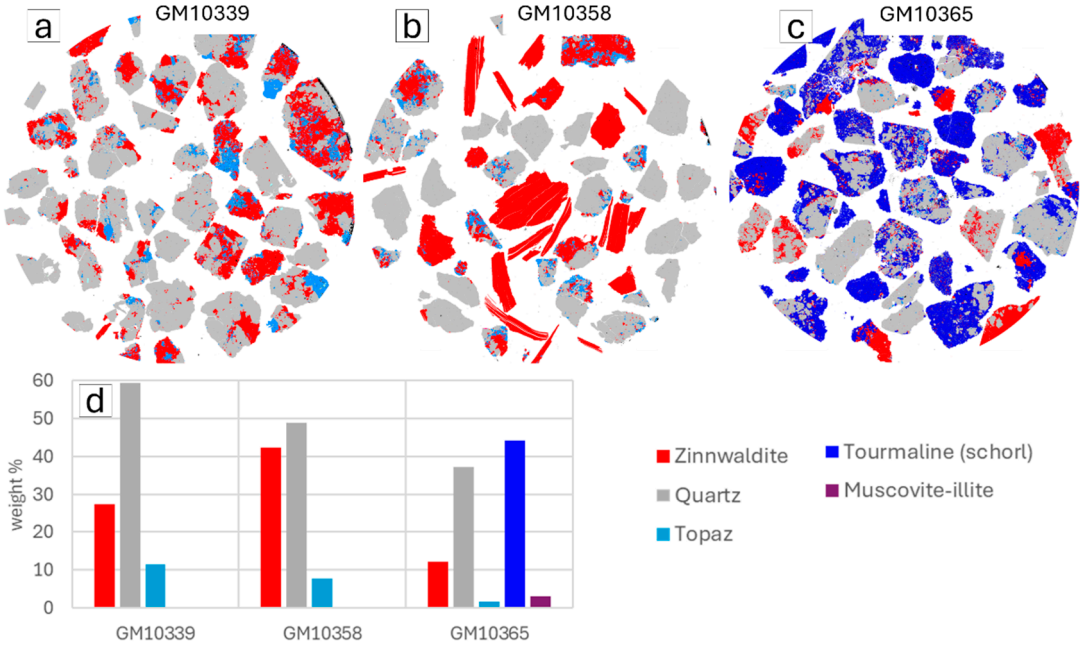

Figure 6. Examples of automated mineralogy results for 25 mm diameter grain mounts. (**a**–**c**): images of grain mounts. (**d**) Bar graph illustrating the weight percentage of minerals in the grain mounts. Corresponding data are provided in Table 3.

3.2.2. Liberation

Although the images in Figure 6 are illustrative and not representative, they confirm that at least some of the Li-bearing mica (zinnwaldite) is liberated. This is most evident in sample GM10358, where vein-hosted zinnwaldite shows ~61% of grains falling into the 95–100% liberation class (Figure 7). Grain size distribution data (Figure 8) further support this, indicating that only ~29% of the Li-mica grains in GM10358 are smaller than 1200 µm.

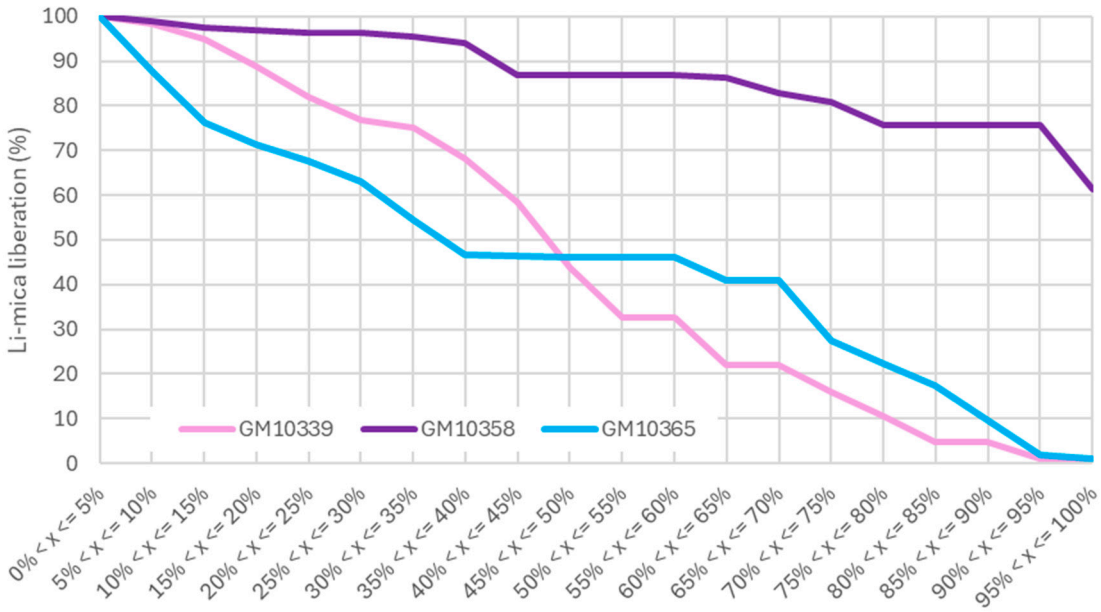

Figure 7. Example plot of liberation data for Li-bearing mica (zinnwaldite). The x-axis represents liberation classes in 5% increments.

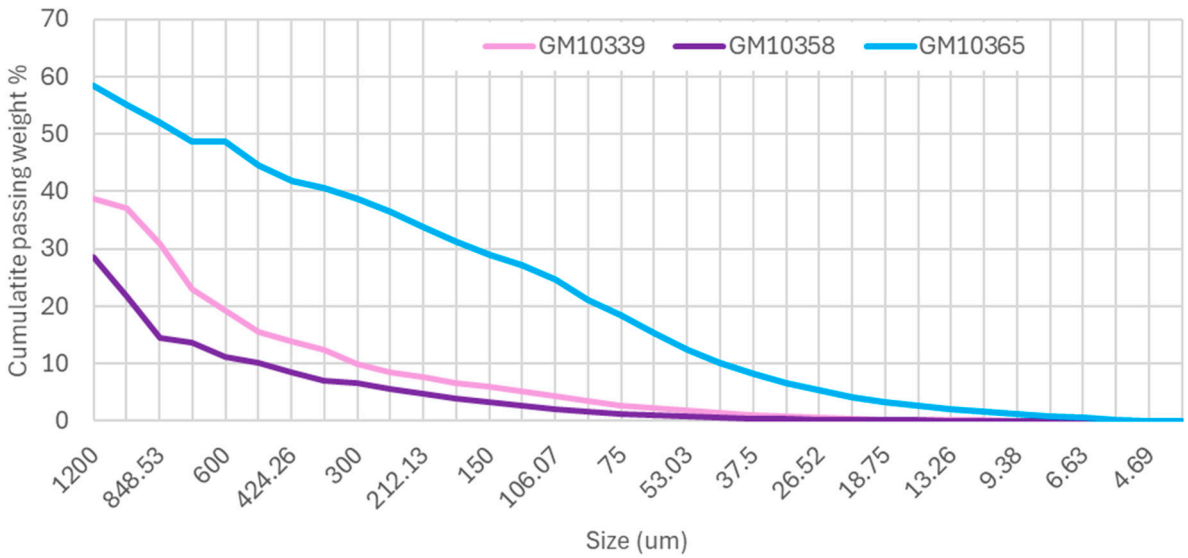

Figure 8. Example plot showing the cumulative grain size distribution of Li-bearing mica (zinnwaldite) for the samples shown in Figure 6. The x-axis represents the sieve size series used in the AMICS analysis. Coarse grains dominate in all samples.

3.2.3. Association

Zinnwaldite is associated with quartz, topaz, and muscovite-illite in all samples (Figure 9; Table 4). In GM10358, a higher proportion of zinnwaldite exhibits free surface (i.e., it appears liberated, at least in two dimensions), and this mineral shows a slightly stronger association with topaz. In contrast, in GM10365, zinnwaldite is primarily associ-

ated with schorl (tourmaline). GM10339 additionally shows zinnwaldite associated with fluorite.

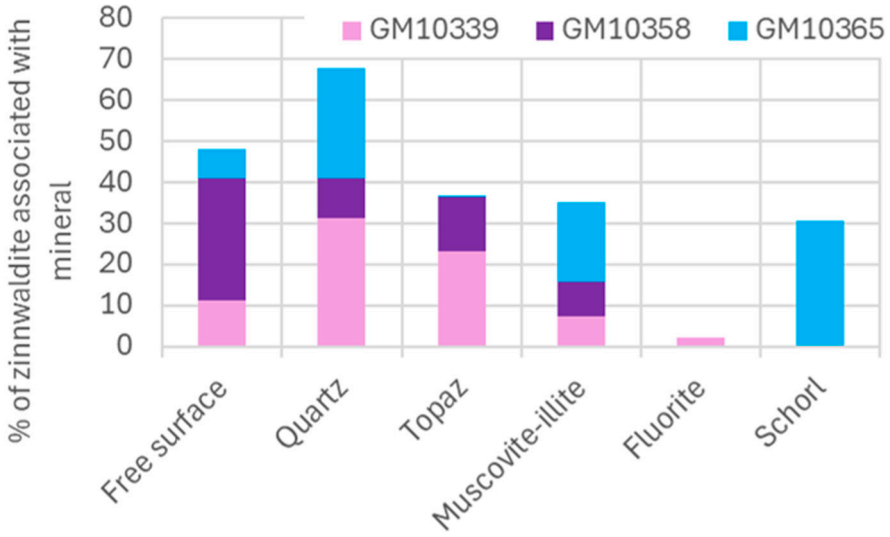

Figure 9. Mineral associations of zinnwaldite in each sample. The graph shows the percentage of total zinnwaldite surface area associated with either a free surface or another mineral based on two-dimensional SEM-AMICS analysis. Corresponding data are provided in Table 4.

Table 4. Percentage of the total zinnwaldite surface area in each sample associated with either a free surface or specific minerals in each sample based on two-dimensional SEM-AMICS analysis.

Sample	Free Surface	Quartz	Topaz	Muscovite-Illite	Fluorite	Tourmaline (Schorl)
GM10339	11.19	31.37	23.31	7.40	2.15	0.08
GM10358	29.74	9.58	13.14	8.47	0	0.08
GM10365	7.06	26.99	0.45	19.47	0	30.47

3.3. Element Distribution

3.3.1. SEM-AMICS Data

SEM-based automated mineralogy data indicate that zinnwaldite accounts for up to ~68% of the fluorine (F) content in the samples, with the remainder hosted by topaz, fluorite, and muscovite-illite (Figure 10).

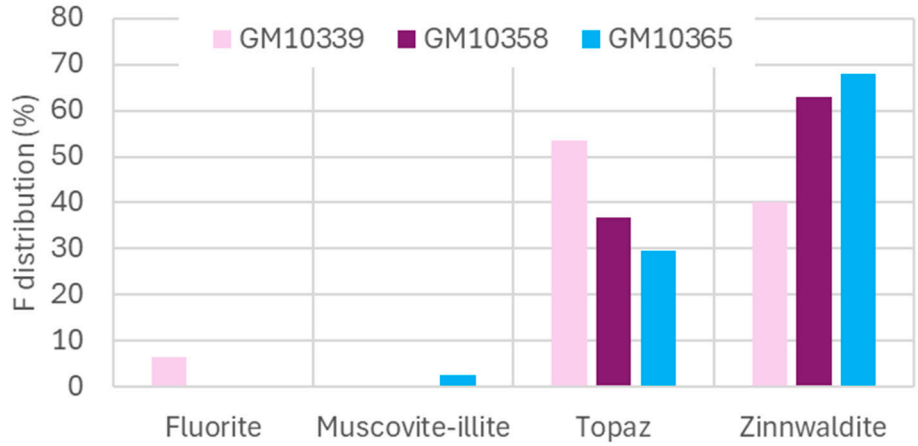

Figure 10. Distribution of F among mineral phases in the analyzed samples based on SEM-AMICS data. Zinnwaldite accounts for the highest proportion of total F, followed by topaz, fluorite, and muscovite-illite.

3.3.2. LA-ICP-MS Data

The LA-ICP-MS spot analyses reveal the following trace element ranges in zinnwaldite in the Tasmanian greisen samples: 8000–16,100 ppm Li (1.7%–3.5% Li_2O); 4000–11,900 ppm Rb (0.4%–1.3% Rb_2O); and 100–1300 ppm Cs (0.01%–0.1% Cs_2O). The element concentrations differ between the vein-hosted and groundmass mica (Figure 11). Groundmass mica generally exhibits a wider range of values and contains higher Rb, Cs, and REE (La, Ce, Pr, and Nd) contents but lower Li compared to vein-hosted zinnwaldite. The distribution of elements within zinnwaldite is heterogeneous. For instance, Rb is typically uniformly distributed, whereas in at least some mica samples, REEs are enriched along cleavage planes and in inclusions (Figure 12). Some Li-bearing mica also contains Bi, which is also enriched along cleavage planes and in inclusions (Figure 12d). These inclusions primarily consist of Bi-Cu-Th-As (Figure 13) and are more commonly found in vein-hosted zinnwaldite than in groundmass mica (Figure 14).

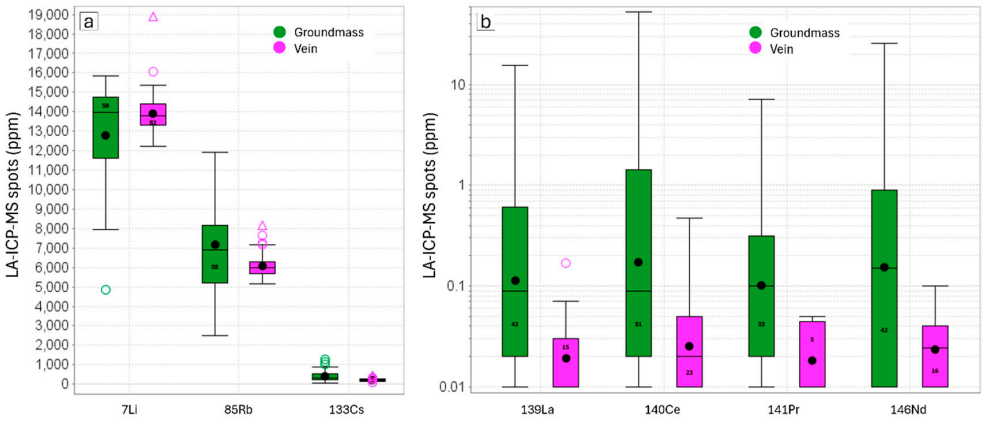

Figure 11. Plot showing the range of Li, Rb, and Cs values (**a**) and REEs (**b**) measured in LA-ICP-MS spots within Li-bearing mica from vein-hosted and groundmass occurrences. Black circles indicate mean values for each group. Open circles and open triangles indicate outliers and far outliers respectively.

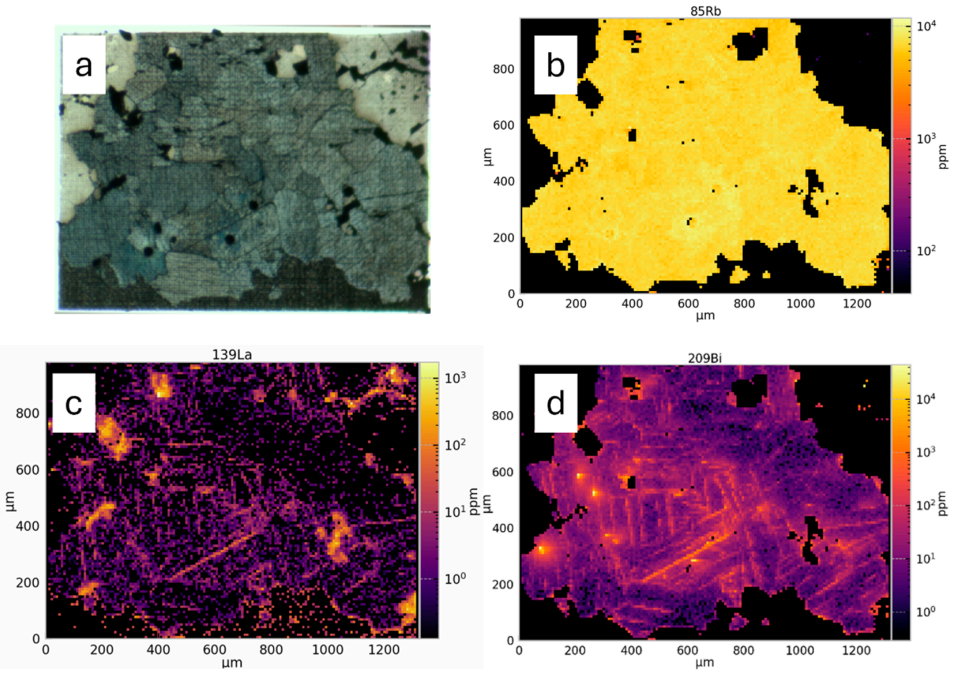

Figure 12. LA-ICP-MS element distribution maps for a representative groundmass zinnwaldite grain. (**a**) Reflected light image of the analyzed grain; (**b**) Rb distribution; (**c**) La distribution; and (**d**) Bi distribution.

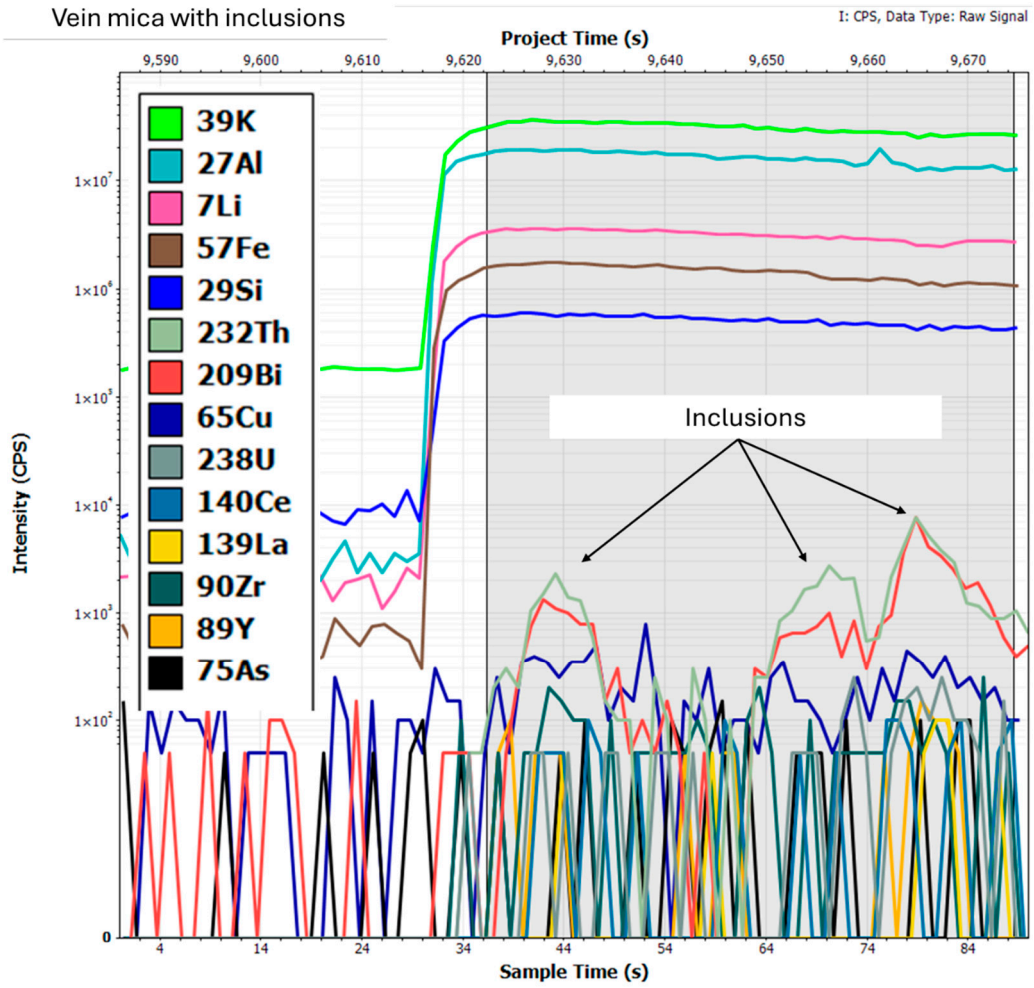

Figure 13. Example of LA-ICP-MS spot analysis of vein-hosted mica showing multiple Bi-Cu-Th inclusions.

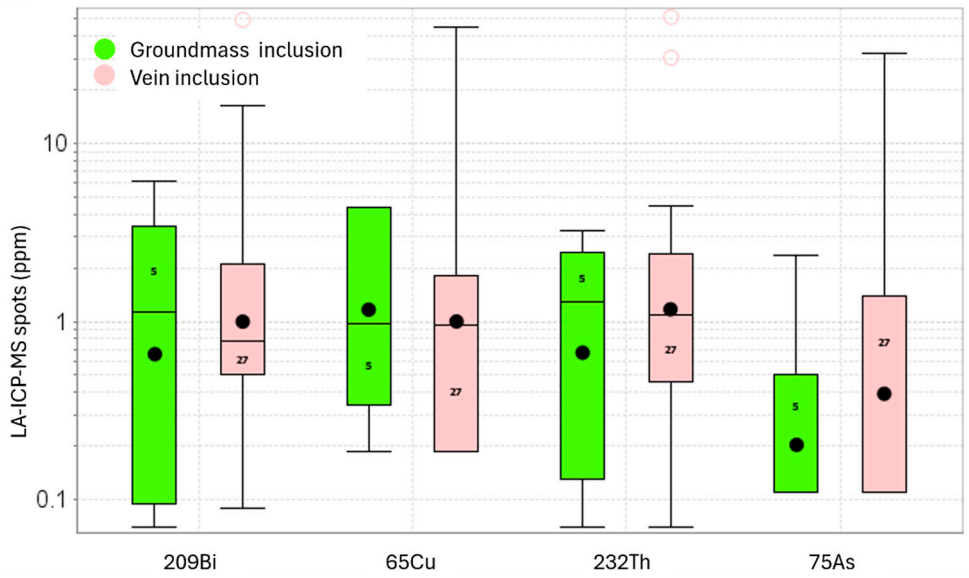

Figure 14. Results of LA-ICP-MS spot analyses of inclusions within Li-bearing mica. A total of five inclusions were identified in groundmass mica and 27 inclusions in vein-hosted mica. Black circles indicate mean values for each group. Open circles indicate outliers.

4. Summary and Conclusions

This study investigated hard, dense, finely crystalline greisen and greisen cross-cut by coarsely crystalline mica veins from northeastern Tasmania. The samples are predominantly composed of quartz, topaz, and mica ± tourmaline (Figure 6). Lithium occurs in zinnwaldite, a Li-bearing mica present both in the groundmass and in cross-cutting veins. The zinnwaldite also hosts the critical elements Rb and Cs (Figure 11), with grades comparable to those of well-documented deposits. For instance, zinnwaldite from the Degana deposit contains ~5000 to 8000 ppm Rb and ~90 to 300 ppm Cs with Li content from ~3400 to 6100 ppm [29], while samples from the Cínovec deposit contain ~2.0–4.4 wt% Li_2O and 0.8–1.9 wt% Rb_2O [30].

EPF was selected as the comminution method due to its reported ability to promote breakage along grain boundaries and enhance mineral liberation [10–18]. By adjusting the operating parameters, EPF effectively fragmented the study samples and liberated and preserved the coarse-grained nature of zinnwaldite. Visual inspection and SEM-based mineralogical analyses of the fragmented samples indicate that at least some breakage occurred along the mineral boundaries, particularly in coarsely crystalline mica, thereby preserving its natural coarse-grained size (Figure 4). While not fully representative, SEM-based mineralogical analyses clearly show that at least some of the mica is liberated. For example, for coarsely crystalline mica, ~61% of the zinnwaldite is 95–100% liberated (Figure 7). However, EPF performance is known to vary with rock texture, mineralogy, and physical properties [16,18], so a more extensive test program is recommended.

SEM-based automated mineralogy indicates that Li occurs within zinnwaldite. LA-ICP-MS spot analyses reveal Li concentrations of 8000 to 16,100 ppm, with vein-hosted zinnwaldite generally showing higher Li content than groundmass mica. Groundmass mica, in turn, showed higher contents of Rb, Cs, and REEs (La, Ce, Pr, and Nd; Figure 11). SEM-AMICS data indicate that zinnwaldite hosts up to 68% of the sample's fluorine (F) content, with additional F present in topaz, fluorite, and muscovite-illite (Figure 10).

Trace elements within zinnwaldite display heterogeneous distribution. For example, Rb is typically uniformly distributed, whereas REEs and Bi tend to occur along cleavage planes and in Bi-Cu-Th-As mineral inclusions (Figure 12). These inclusions are more abundant in vein-hosted zinnwaldite than in groundmass zinnwaldite (Figure 14).

In summary, zinnwaldite-bearing greisen from northeastern Tasmania contain critical metal grades (Li, Rb, and Cs) comparable to those of economically significant European deposits. Additionally, zinnwaldite hosts elevated levels of REEs and Bi, which have the potential to be co- or by-products. While further work is needed, these samples may be suitable for recently developed leaching processes designed for extracting Li from Li micas, such as the combined L-Max® and LOH-Max® processes, developed by [31], which are currently being tested by [32], or the CO_2 leaching (COOL) process [33].

Author Contributions: Conceptualization, J.H.; formal analyses, J.H, J.O., M.A. and S.F.; writing, review and editing, J.H., J.O., M.A., E.P., R.F., and S.F. All authors have read and agreed to the published version of the manuscript.

Funding: The authors acknowledge support from the project 'Building capacity in Regional Australia to enhance Australia's Economy through research, training, and environmentally sustainable production of critical metals', a Regional Research Collaboration (RRC) project supported by the Australian Government Department of Education. Funding was provided to CODES, University of Tasmania.

Data Availability Statement: All data presented in this study are available upon contact with the corresponding author.

Acknowledgments: The authors would like to thank the staff of TinOne Resources Inc. for providing access to samples, the staff at GeMMe, University of Liege, for their assistance with analyses and access to equipment, and the staff at CODES labs and the Central Science Laboratory, University of Tasmania, for their support with analyses and data processing. Finally, we would like to express huge thanks to the above and all our collaborators and colleagues for their support of the RRC project.

Conflicts of Interest: The authors declare that they have no known conflicts of interest. Author Russell Fulton was employed by the company TinOne Resources Inc, a company assisting in the 'Building capacity in Regional Australia to enhance Australia's Economy through research, training, and environmentally sustainable production of critical metals' project through a non-financial agreement. The remaining authors declare that the research was conducted in the absence of any commercial or financial relationships that could be construed as a potential conflict of interest.

References

1. Pehlken, A.; Albach, S.; Vogt, T. Is there a resource constraint related to lithium ion batteries in cars? *Int. J. Life Cycle Assess.* **2017**, *22*, 40–53. [CrossRef]
2. Brunelli, K.; Lee, L.; Moerenhout, T. Fact Sheet: Lithium Supply in the Energy Transition. Centre on Global Energy Policy Website. Available online: https://www.energypolicy.columbia.edu/publications/fact-sheet-lithium-supply-in-the-energy-transition/ (accessed on 3 March 2025).
3. Critical Minerals at Geoscience Australia. Geoscience Australia Website. Available online: https://www.ga.gov.au/scientific-topics/minerals/critical-minerals (accessed on 2 December 2024).
4. Grohol, M.; Veeh, C. *Study on the Critical Raw Materials for the EU 2023—Final Report*; Publications Office of the European Union European Commission, Directorate-General for Internal Market, Industry, Entrepreneurship and SMEs, Publications Office of the European Union: Luxembourg, 2003; ISBN 978-92-68-00414-2. [CrossRef]
5. List of Critical Minerals. United States Geological Survey Website. Available online: https://www.usgs.gov/news/national-news-release/us-geological-survey-releases-2022-list-critical-minerals (accessed on 2 December 2024).
6. Cinovec Lithium Project Update. European Metals Holdings Limited Website. Available online: https://api.investi.com.au/api/announcements/emh/387cfa8b-b66.html (accessed on 2 December 2024).
7. Zinnwald Lithium Project. Zinnwald Lithium Website. Available online: https://zinnwaldlithium.com/project/the-resource/ (accessed on 2 December 2024).
8. Announcement May 2023, Testwork Realizes Continued Outstanding Lithium Recoveries. European Metals Holdings Limited Website. Available online: https://www.europeanmet.com/announcements/ (accessed on 3 March 2025).
9. Process Metallurgy. British Lithium Website. Available online: https://imerysbritishlithium.com/process-metallurgy/ (accessed on 1 April 2025).
10. Andres, U.; Jirestig, J.; Timoshkin, I. Liberation of minerals by high-voltage electrical pulses. *Powder Technol.* **1999**, *104*, 37–49. [CrossRef]
11. Ménard, Y. Energy Savings in Comminution—Innovative Routes for Mineral Ores Embrittlement. Contribution to Deliverable 4.4—Promine Project (FP7). BRGM/RP-60127-FR. 2011. 36p. Available online: https://infoterre.brgm.fr/rapports/RP-60127-FR.pdf (accessed on 1 April 2025).
12. Sperner, B.; Jonckheere, R.; Pfänder, J.A. Testing the influence of high-voltage mineral liberation on grain size, shape and yield, and on fission track and 40Ar/39Ar dating. *Chem. Geol.* **2014**, *371*, 83–95. [CrossRef]
13. Rudashevsky, N.S.; Weiblen, P.W.; Stoynov, H.; Saini-Eidukat, B. Products of electric pulse desaggregation of some Keweenawan rocks. In Proceedings of the Institute on Lake Superior Geology 41st Annual Meeting, Marathon, ON, Canada, 13–18 May 1995; Volume 41, p. 61.
14. Saini-Eidukat, B.; Weiblen, W. A New Method of Fossil Preparation, Using High-Voltage Electric Pulses. *Curator* **1996**, *39*, 139–144. Available online: https://www.ndsu.edu/pubweb/~sainieid/PPD/Saini-Eidukat-and-Weiblen-Liberation-of-Fossils-using-Electric-Pulses.pdf (accessed on 1 April 2025). [CrossRef]
15. Andres, U. Development and prospects of mineral liberation by electrical pulses. *Int. J. Miner. Process.* **2010**, *97*, 31–38. [CrossRef]
16. Wang, E.; Shi, F.; Manlapig, E. Pre-weakening of mineral ores by high voltage pulses. *Miner. Eng.* **2011**, *24*, 455–462. [CrossRef]
17. Wang, E.; Shi, F.; Manlapig, E. Mineral Liberation by High Voltage Pulses and Conventional Comminution with Same Specific Energy Levels. *Miner. Eng.* **2012**, *27–28*, 28–36. [CrossRef]
18. van der Wielen, K.P.; Pascoe, R.; Weh, A.; Wall, F.; Rollinson, G. The influence of equipment settings and rock properties on high voltage breakage. *Miner. Eng.* **2013**, *46–47*, 100–111. [CrossRef]

19. Lyons, R.J.P. The Aberfoyle vein system, Rossarden, Tasmania. In Proceedings of the AUSIMM, Sydney, Australia, 10–15 August 1957; No. 181. pp. 75–91. Available online: https://www.ausimm.com/publications/conference-proceedings/the-ausimm-proceedings-1957/the-aberfoyle-vein-system-rossarden-tasmania/ (accessed on 2 December 2024).
20. Seymour, D.B.; Green, G.R.; Calver, C.R. *The Geology and Mineral Deposits of Tasmania: A Summary*; Mineral Resources Tasmania Geological Survey Bulletin: Hobart, Australia, 2006.
21. TinOne Resources Inc. Aberfoyle Tin Project. Available online: https://tinone.ca/ (accessed on 8 October 2024).
22. Müller, A.; Herklotz, G.; Giegling, H. Chemistry of quartz related to the Zinnwald/Cínovec Sn-W-Li greisen-type deposit, Eastern Erzgebirge, Germany. *J. Geochem. Explor.* **2018**, *190*, 357–373. [CrossRef]
23. High Voltage Pulse Power Machines. SELFRAG Website. Available online: https://www.selfrag.com/high-voltage-pulse-power-machines (accessed on 3 March 2024).
24. AMICS Automated Mineralogy System for SEM. Bruker Website. Available online: https://www.bruker.com/en/products-and-solutions/elemental-analyzers/eds-wds-ebsd-SEM-Micro-XRF/software-amics-automated-mineralogy-system.html (accessed on 3 March 2024).
25. Jochum, K.P. Determination of reference values for NIST SRM 610–617 glasses following ISO guidelines. *Geostand. Geoanalytical Res.* **2011**, *35*, 397–429. [CrossRef]
26. GeoReM Preferred Values. GeoRem Website. Available online: http://georem.mpch-mainz.gwdg.de/ (accessed on 24 September 2024).
27. Longerich, H.P.; Jackson, S.E.; Günther, D. Inter-laboratory note—Laser ablation inductively coupled plasma mass spectrometric transient signal data acquisition and analyte concentration calculation. *J. Anal. At. Spectrom.* **1996**, *11*, 899–904. [CrossRef]
28. Norris, A.; Danyushevsky, L. Towards estimating the complete uncertainty budget of quantified results measured by LA-ICP-MS. In Proceedings of the Goldschmidt Conference, Boston, MA, USA, 12–17 August 2018.
29. Ghosh, U.; Upadhyay, D.; Mishra, B.; Abhinay, K. In-situ trace element and Li-isotope study of zinnwaldite from the Degana tungsten deposit, India: Implications for hydrothermal tungsten mineralization. *Chem. Geol.* **2023**, *632*, 121550. [CrossRef]
30. Breiter, K.; Hložková, M.; Korbelová, Z.; Galiová, M.V. Diversity of lithium mica compositions in mineralized granite-greisen system: Cinovec Li-Sn-W deposit, Erzgebirge. *Ore Geol. Rev.* **2019**, *106*, 12–27. [CrossRef]
31. Technologies Leading the Next Lithium Cycle. Lepidico Website. Available online: https://lepidico.com/technology (accessed on 2 December 2024).
32. Processing Technology. Cornish Lithium Website. Available online: https://cornishlithium.com/projects/lithium-in-hard-rock/processing-technology/ (accessed on 2 December 2024).
33. Mende, R.; Kaiser, D.; Pavon, S.; Bertau, M. The COOL process: A holistic approach towards lithium recycling. *Waste Biomass Valorization* **2023**, *14*, 3027–3042. [CrossRef]